(Received 9 December 2025, Accepted 21 January 2026, Scheduled 10 February 2026)

High-Gain Dual Band MIMO Antenna Using Metamaterial Surface for Bluetooth, Wi-Fi and 5G Applications

Nilesh Lakade[1,2], Shankar D. Nawale[3], Anjali Rochkari[4], Mahadu Trimukhe[5], and Rajiv Gupta[6,*]

[1]S. K. N. Sinhgad College of Engineering, Pandharpur, Solapur, India
[2]K. J. Somaiya School of Engineering, Somaiya Vidyavihar University, Mumbai, India
[3]N. B. Navale Sinhgad College of Engineering, Solapur, India
[4]Terna Engineering College, Navi-Mumbai, India
[5]Bharati Vidyapeeth (Deemed to be University), DET (Off Campus), Navi Mumbai, India
[6]Ramrao Adik Institute of Technology, D. Y. Patil Deemed to be University, Navi-Mumbai, India

ABSTRACT: In this paper, an elliptical monopole antenna is operated in the fundamental mode by reducing the electromagnetic coupling (EMC) between higher-order modes. The electromagnetic coupling is decreased by decreasing the width of the radiating element and ground-plane dimensions, and by increasing the gap between the radiating element and the ground plane. The ellipse is sliced from the top, as there is little surface current on the top portion of the monopole. The symmetrical portion of this sliced elliptical monopole is selectively etched with little effect on impedance variation. Dual-band characteristics are obtained over 2.3–2.7 GHz (Wi-Fi and Bluetooth bands) and 5.4–5.9 GHz (WLAN band), as well as over 2.3–2.7 GHz (Wi-Fi and Bluetooth bands) and 5.13–5.71 GHz (WLAN band), depending on the etching amount. A rectangular strip is added to the etched monopole to operate over 2.3–2.7 GHz (Wi-Fi, Bluetooth bands) and 3.3–3.9 GHz (5G band). To enhance the gain of the compact dual-band antenna, a reflecting metamaterial surface consisting of an array of square patches is designed and placed below the structure. A high-gain dual-band MIMO antenna is designed by placing four elements orthogonally above the center of the four edges of the metamaterial surface. $S_{11} < -10$ dB, isolation > 18 dB and 22 dB, and antenna gain of 7.5 dBi and 7.4 dBi are obtained over 2.35–2.7 GHz and 3.3–3.6 GHz, respectively. The structure is fabricated. The measurement results validate the simulation ones.

1. INTRODUCTION

Wireless technology has evolved and continues to grow to meet the increasing demands for high data rates, reliability, low latency, and uninterrupted connectivity. Wi-Fi, Bluetooth, and 5G technologies have become essential for enhancing productivity, driving business growth, supporting economic development, and improving entertainment and comfort. Virtual and augmented reality, and video streaming have transformed our experiences. The significant impact of 5G technology on our daily lives and socioeconomic landscape has prompted researchers to enhance its functionality and performance, reduce cost, miniaturize size, and expand 5G networks. This has driven the development of novel antennas for 5G, Wi-Fi, WLAN, and Bluetooth applications.

A monopole antenna offers an ultra-wide bandwidth (UWB) as the fundamental mode, and higher-order modes get excited and electromagnetically couple with other modes. A monopole antenna offers an omnidirectional radiation pattern. However, the gain and radiation patterns vary over the UWB [1, 2]. Multiband monopole antennas operate over a number of desirable bands and thus have better functionality, low cost, and occupy less space than a number of antennas operating over individual bands.

Various techniques have been employed to design multiband antennas. An antenna with multiple branches offers multiband operation as different branches resonate at different frequencies [3–5]. Multiband antennas are designed by etching slots in a patch or ground plane [6–8]. A compact dual-band antenna has evolved by etching slots in a rectangular monopole for 5G applications [9]. The fractal technique is used to design multiband antennas in [10, 11]. However, there are applications in which directional antennas are required.

The gain of the monopole antennas is improved by using reflective layers. Frequency Selective Surface (FSS) or metamaterial surfaces are designed to reflect the radiating fields and are placed at a distance from the monopole radiator to cause constructive interference with direct radiating fields to enhance the antenna gain [12–20]. A comprehensive study of the gain enhancement of UWB antennas is reported in [12]. 8.3 dBi gain is obtained over 3–12 GHz using FSS [13]. A $1.3\lambda \times 1.3\lambda$ curved FSS layer is used to enhance the gain of a UWB antenna over 2.66–17.98 GHz, achieving a peak gain of 12 dBi [14]. Gain enhancement of the UWB antenna using an FSS by applying machine learning technique is reported in [15]. However, radiation patterns vary over the bandwidth. FSS is also employed to improve the gain of dual-band monopole antennas in [16, 17]. However, these antennas have large FSS dimensions.

An artificial magnetic conductor (AMC) reflecting surface is designed to enhance the gain of a coplanar-waveguide

* Corresponding author: Rajiv Gupta (rajiv.gupta@dypatil.edu).

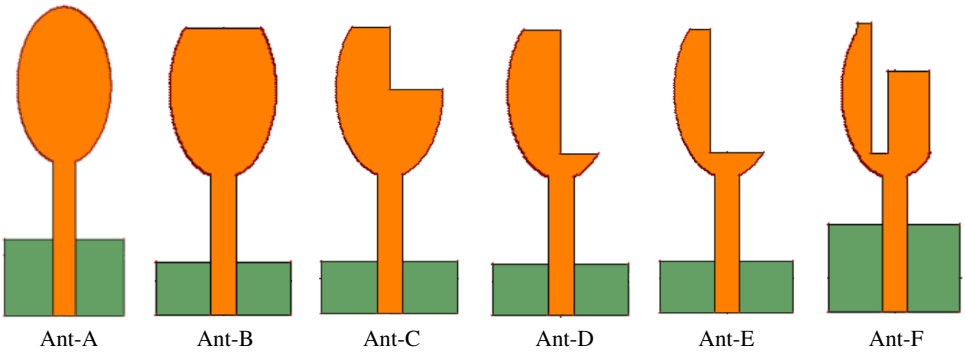

FIGURE 1. Different stages of development of a dual-band antenna.

(CPW)-fed dual-band (2.37–2.5 GHz and 4.45–4.9 GHz) split-ring monopole antenna. The peak gains of 5 dBi and 7.5 dBi are obtained over two bands [18]. A metamaterial surface (MS) consisting of a 3×3 array of split-ring unit cells is placed at 0.33λ from a UWB monopole to achieve 8.3 dBi peak gain [19]. A metallic reflector is used to increase the gain of a 5G mm-wave antenna for high-speed railway communication [20].

Multiple-input multiple-output (MIMO) antennas have been proven to be the backbone of 5G technology, supporting various industrial, medical, transportation, and environmental applications. MIMO technology results in a high data rate and low latency [21]. In compact devices, mutual coupling degrades the performance of the MIMO antennas. T-shaped decoupling structure [22], neutralization-lines, stubs, and slots [23] are used to enhance isolation. However, an oval-shaped MIMO antenna with a slot and rings [24] and a 4-element MIMO antenna designed using a hybrid-shaped monopole with a circular slot and a strip [25] have achieved good isolation without the use of any isolation structure.

Here, a dual-band antenna to operate over 2.3–2.7 GHz and 3.3–3.9 GHz for Bluetooth, Wi-Fi, and 5G sub-6 GHz applications is designed. A reflecting MS is placed below the antenna. The maximum gains of 7.5 dBi at 2.5 GHz and 7.4 dBi at 3.45 GHz are obtained. The 4-element high-gain MIMO antenna with isolation > 18 dB is proposed for 5G applications. High-gain MIMO antennas also find applications in radio frequency (RF) energy harvesting for recharging wireless sensors and devices [26].

2. DESIGN THEORY AND ANTENNA GEOMETRY

The electromagnetic (EM) coupling between fundamental and higher-order modes depends on the shape and width of the radiator, ground-plane dimensions, and the gap between the radiator and ground plane. An elliptical monopole antenna is operated in the fundamental mode by decreasing the EMC between the fundamental and higher-order modes. The EMC is decreased by decreasing the width of the radiating element and ground-plane dimensions, and by increasing the gap between the ground plane and radiating element. The surface current decreases from the feed to the top edge of the monopole radiator. Therefore, the top portion of the elliptical monopole is etched with little effect on the impedance bandwidth (BW) of the monopole. The symmetrical part of an elliptical monopole can also be selectively etched with a negligible effect on the impedance BW. The selective etching from the top and the right, to some extent, does not affect the impedance BW of the monopole; however, dual-band characteristics are obtained over 2.3–2.7 GHz (Wi-Fi, Bluetooth bands) and 5.4–5.9 GHz (WLAN band), as well as over 2.3–2.7 GHz (Wi-Fi, Bluetooth bands) and 5.13–5.71 GHz (WLAN band), depending on the amount of etching. A rectangular strip is added to the etched monopole to operate it over 2.3–2.7 GHz (Wi-Fi, Bluetooth bands) and 3.3–3.9 GHz (5G band).

The gain of the dual-band antenna is enhanced using a reflective metamaterial surface consisting of an array of square patches whose dimensions and periodicity are $< 0.1\lambda_0$, where λ_0 is the free-space wavelength at the highest operating frequency. The AMC surface is placed at a distance such that the reflecting fields and direct radiating fields are in phase, to improve the gain of the antenna over both bands. The four dual-band antenna elements are placed orthogonally at the center of the edge of the AMC surface to design a high-gain dual-band MIMO antenna.

2.1. Evolution of Dual-Band Antenna

The dual-band antenna is derived from an elliptical monopole antenna. The different stages of development are shown in Fig. 1. The scalar and vector surface current densities of these stages at their resonant frequencies are shown in Fig. 2. The geometry of the dual-band antenna, along with the detailed parameters and dimensions, is presented in Fig. 3.

Initially, an elliptical monopole antenna (EMPA), with a major axis length of $a = 21.0$ mm, a minor axis length of $b = 12.4$ mm, and a gap between the EMPA and ground $g = 10$ mm, is designed on a 1.6 mm thick FR4 substrate ($\varepsilon_r = 4.4$, $\tan\delta = 0.02$) using the IE3D simulator. The length and width of the ground plane are $Lg = 16$ mm and $Wg = 10.2$ mm, respectively. This antenna is referred to as 'Ant-A'. The surface current flows along the edge of the EMPA. The lowest operating frequency (f_L), corresponding to $S_{11} = -10$ dB of 'Ant-A', depends on the current path length from the ground plane edge to the top of the EMPA and is given by [1].

$$f_L = 72/\left(0.25\pi(a+b)+g\right) \quad (1)$$

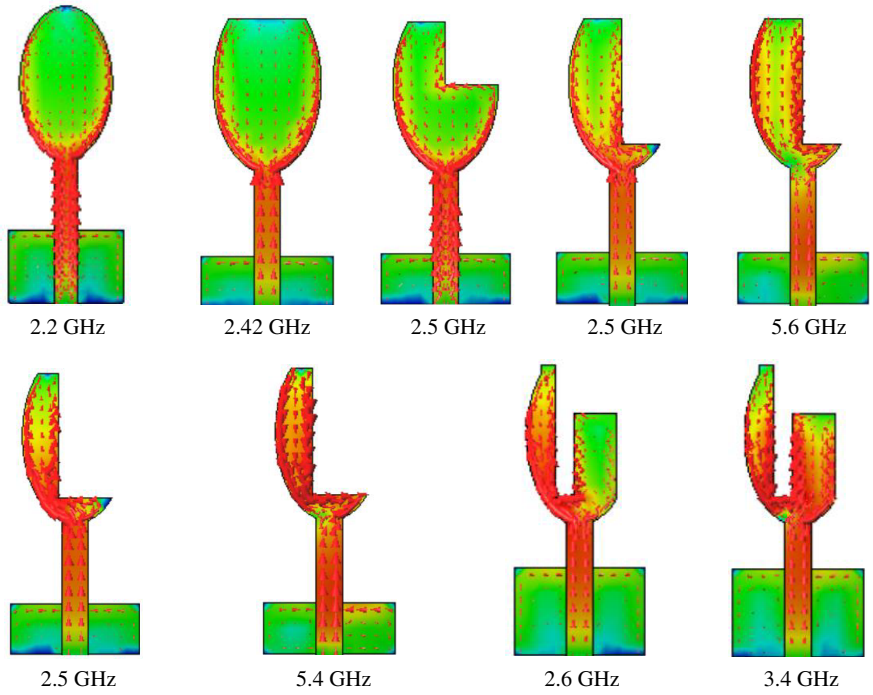

FIGURE 2. Scalar and vector surface current densities of different stages at their resonant frequencies.

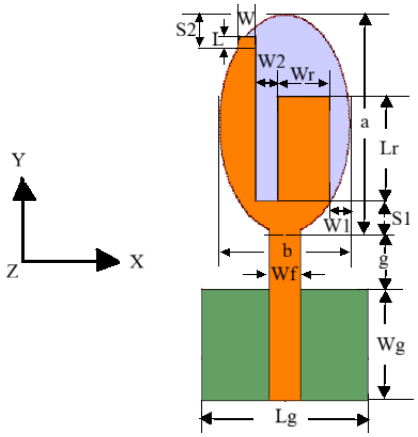

FIGURE 3. Geometry of the proposed dual-band antenna designed by etching the selective portion of the elliptical monopole ($Lg = 16$, $Wg = 10.7$, $g = 5.5$, $a = 21$, $b = 12.4$, $Wf = 3$, $S1 = 3.1$, $S2 = 3.1$, $Lr = 14.2$, $Wr = 5$, $L = 1.0$, $W = 1.7$, $W1 = 2.0$, $W2 = 2.1$). All dimensions are in mm.

The theoretical value of f_L using (1) is 1.987 GHz, whereas the simulated f_L is 2.015 GHz. The EMPA resonates mainly in the fundamental mode with a minimum $S_{11} < -35$ dB. As the surface current density is not uniform along the edge and decreases from the feed point to the top edge of the EMPA (Fig. 2), the effective current path length decreases. Therefore, the fundamental resonant frequency is higher than f_L. The resonant frequency and impedance bandwidth also depend on the ground plane dimensions. The EMC between the fundamental and higher-order modes is decreased by increasing 'g' and decreasing the width of the radiating element 'b' ($b < a$) and the ground-plane dimensions so that the EMPA resonates in the fundamental mode.

Since there is little current at the top portion of the EPMA; therefore, EPMA is etched from the top by 3.1 mm (about 15% of the major axis length 'a') with little effect on the impedance BW of the monopole. The ground plane width is decreased to 6.2 mm. This antenna is termed 'Ant-B'. A decrease in the ground-plane width decreases the inductive impedance and increases the resistance of the structure. Therefore, the impedance variation plot shifts downward and towards the right, and the resonant frequency increases in Ant-B. $S_{11} < -10$ dB is obtained over 2.23–2.68 GHz. The geometry and surface current density of Ant-B are symmetrical along the Y-axis; therefore, a quarter part (right-top) of Ant-B is etched with little effect on the impedance of the structure. This antenna is termed 'Ant-C'. $S_{11} < -10$ dB is obtained over 2.31–2.77 GHz. S_{11} and impedance variation plots of 'Ant-A', 'Ant-B', and 'Ant-C' are shown in Fig. 4.

The symmetrical part in 'Ant-B' is further etched to about 85% of the elliptical major axis length. This antenna is termed 'Ant-D'. It increases the surface current density on the radiating monopole and EM coupling; therefore, another loop appears in the impedance variation plot, which results in dual-band characteristics. There is a negligible effect on the lower-band resonant frequency and bandwidth. At 2.4 GHz, the surface current density is greater along the elliptically shaped edge, and the surface current density vectors tend to tilt towards the left edge. At 5.6 GHz, the surface current density is more along the right edge and is significant along both edges, which indicates electromagnetic coupling and a loop on the impedance variation plot. This results in the emergence of another band. The structure exhibits dual-band characteristics. $S_{11} < -10$ dB is obtained over 2.29–2.70 GHz and 5.35–5.96 GHz. This structure is suitable for Bluetooth, Wi-Fi, and WLAN applications. The vertical edge is etched by 2 mm to form 'Ant-E'. The surface

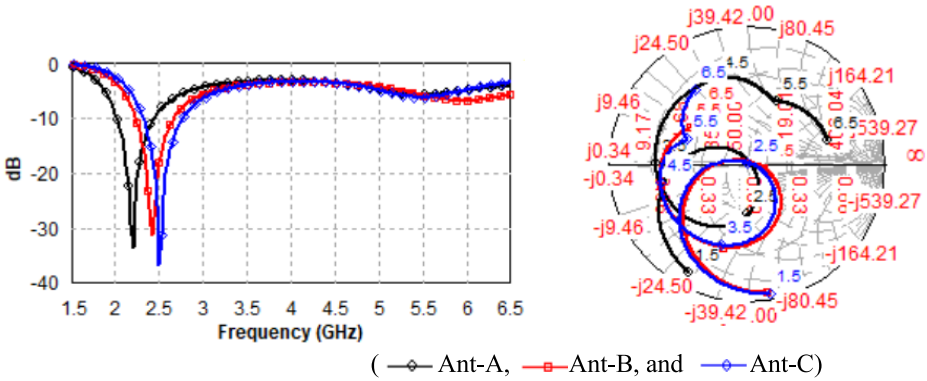

FIGURE 4. S_{11} and impedance variation.

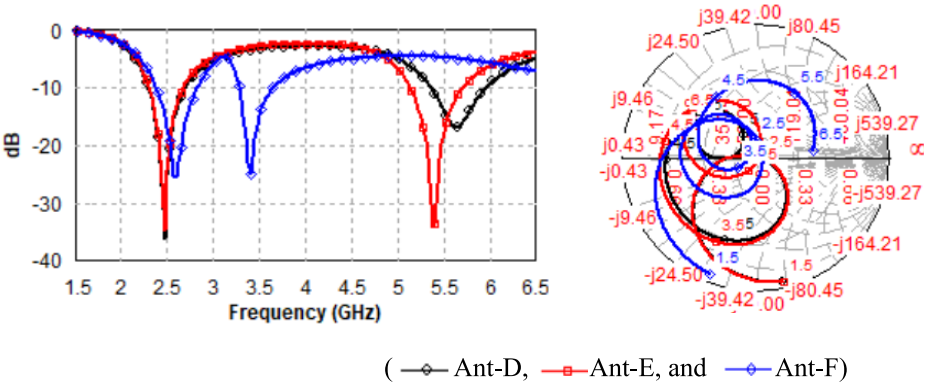

FIGURE 5. S_{11} and impedance variation.

current density increases owing to the decrease in the conducting area. It increases the electromagnetic coupling and, therefore, the loop area on the impedance variation plot. There is a negligible effect on the lower-band resonant frequency, as it is mainly governed by the elliptical edge; however, the upper-band resonant frequency decreases as it depends on the EM coupling and is governed by the right edge. As the effective current path length of the right edge increases, the upper-band resonant frequency decreases. $S_{11} < -10$ dB is obtained over 2.29–2.68 GHz and 5.13–5.71 GHz. This structure is suitable for Bluetooth, Wi-Fi, and WLAN applications. A rectangular strip of 5 mm $\times$ 14.2 mm is added on the right side of 'Ant-D', and a small rectangular patch is added on the top-left side to form 'Ant-E'. The spacing between the rectangular strip and the vertical right edge of 'Ant-D' and 'g' is optimized. $S_{11} < -10$ dB is obtained over 2.38–2.83 GHz and 3.27–3.67 GHz. The proposed dual-band structure operates over Bluetooth, Wi-Fi, and sub-6 GHz 5G bands. The S_{11} and impedance variation plots of 'Ant-D', 'Ant-E', and 'Ant-F' are shown in Fig. 5.

3. HIGH-GAIN DUAL-BAND ANTENNA USING A REFLECTING AMC SURFACE

A metamaterial or AMC surface, considered here, is an array of square patches with periodicity and dimensions less than $0.1\lambda_0$ (λ_0 — wavelength in free space at 3.6 GHz). The AMC surface consisting of an 11 $\times$ 11 array of 7 mm square patches with a periodicity of 9 mm is placed below the designed dual-band antenna 'Ant-F' at height 'H'. The center of the MS coincides with that of the dual-band antenna. The metamaterial surface reflects the fields radiated and directed towards the MS. At a particular height 'H', the fields radiated upward by the monopole interfere constructively with the fields reflected by the MS placed below the monopole antenna. If these fields (radiated upward by the dual-band monopole and reflected from the MS) are in phase, they constructively interfere and enhance the gain of the antenna. The antenna gain depends on the reflection phase, dielectric substrate, and height of the MS from the dual-band antenna [12, 13].

3.1. Reflection Coefficient of AMC Surface

The gain enhancement of the antenna is governed by the reflection coefficient of the AMC surface. The AMC surface, a uniform array of square patches (unit cells) is designed on a 1.6 mm FR4 substrate. Full-wave Floquet analysis is carried out to analyze the unit cell of the AMC surface using the ANSYS-HFSS software, as shown in Fig. 6(a). The resonant frequency of the AMC layer corresponds to 0° reflection phase, whereas the AMC bandwidth corresponds to $\pm 90°$ phase variation. The effect of the unit cell of different patch dimensions 'a' at constant periodicity 'P' and different periodicities 'P' by keeping patch dimensions 'a' fixed at the resonant frequency is analyzed. The metallic patches on the AMC surface act as inductors, and the spacing between the patches acts as a capacitor.

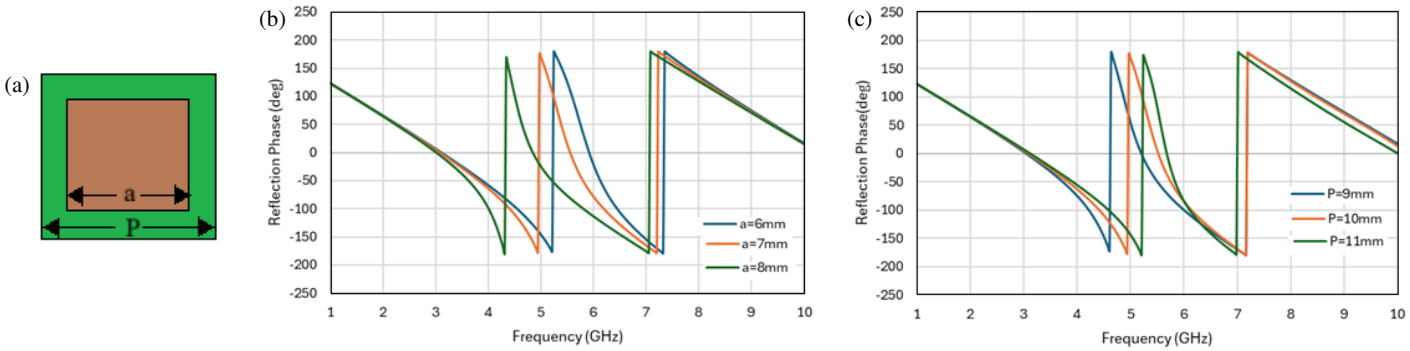

FIGURE 6. (a) AMC unit cell and reflection phase, (b) different 'a', (c) different 'P'.

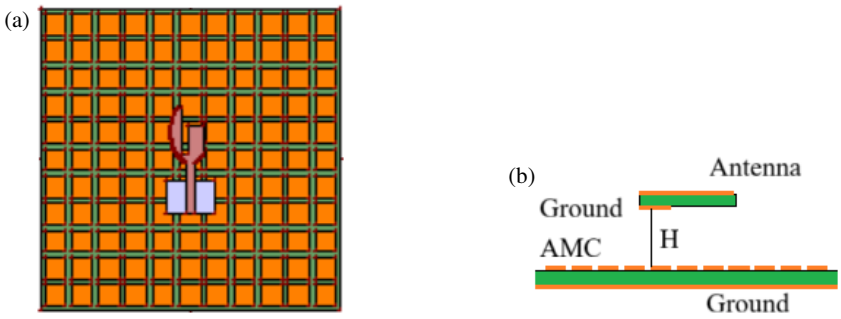

FIGURE 7. Antenna with 11 × 11 array AMC surface. (a) Top view. (b) Side view.

The inductance decreases with a decrease in patch size; therefore, the resonant frequency increases with a decrease in the unit-cell patch dimensions (Fig. 6(b)). As the capacitance decreases, the resonant frequency increases with an increase in the spacing between patches for a constant patch size (Fig. 6(c)). A square patch of side $a = 7$ mm and periodicity $P = 9$ mm is chosen as it offers the desired AMC bandwidth from 2.3 to 3.9 GHz, resonant frequency of 3.1 GHz, and the linear reflection phase variation with frequency over 2.3–3.9 GHz.

3.2. Effect of AMC Surface Height from Monopole Antenna

The AMC surface placed below the antenna acts as a reflecting surface (Fig. 7). The AMC surface increases the gain of the monopole antenna when the fields/waves radiating towards the AMC surface are reflected from it and constructively interfere with the fields/waves radiated by the monopole in the upward direction. The maximum gain is obtained at a particular height when the fields radiated by a monopole in the forward direction are in phase with the fields reflected from the AMC surface.

Assume that ϕf is the phase of the fields transmitted by the monopole in the forward direction, ϕr the phase of the reflected waves, and ϕd the phase delay corresponding to the complete propagation trip from the monopole to the AMC surface and then from the AMC surface to the monopole. If the monopole antenna is placed at a height 'H' from the AMC surface, then for the fields transmitted from the monopole to be in phase with the reflected fields, Equation (2) should be satisfied.

$$\phi f = \phi d + \phi r \quad \text{and} \quad \phi d = 2 \times 2\Pi \times f \times H/c \qquad (2)$$

The AMC surface also loads the monopole antenna. The waves reflected from the AMC surface affect the impedance and impedance matching of the structure. The effect of height on impedance matching and gain is analyzed. As the height between the monopole and AMC surface increases, impedance matching improves in the lower band but degrades slightly in the upper band. The bandwidth increases with an increase in AMC surface height. In the upper band, the resonant frequency and BW increase slightly. As the electrical height ($H\lambda$) increases with an increase in frequency, the loading effect of the AMC surface decreases over the upper band. As the AMC height is varied from the optimum height ($H = 18$ mm), the maximum gain of the antenna decreases over the upper band. S_{11}, and the gain variations for different heights of the AMC surface are shown in Fig. 8. A peak gain of approximately 7.5 dBi is obtained over both bands.

The scalar and vector surface current density distributions on the AMC surface are shown in Fig. 9. The radiated fields from the dual-band antenna incident upon the AMC surface induce surface currents, which in turn, reradiates the fields. At 2.45 GHz, although the magnitude of the surface current is less, it is in phase in most unit cells of the AMC surface. However, at 3.45 GHz, the magnitude of the surface current is greater in the central unit cells than in the cells at the edges; the surface current vectors are in phase in a limited number of cells. The magnitude and in-phase components of the fields radiated/reflected by the AMC unit cells help to improve the gain of the antenna. The vertical component of the surface current enhances the co-polar gain, whereas the horizontal component leads to cross-polarization. The cross-polarization in the upper band is more

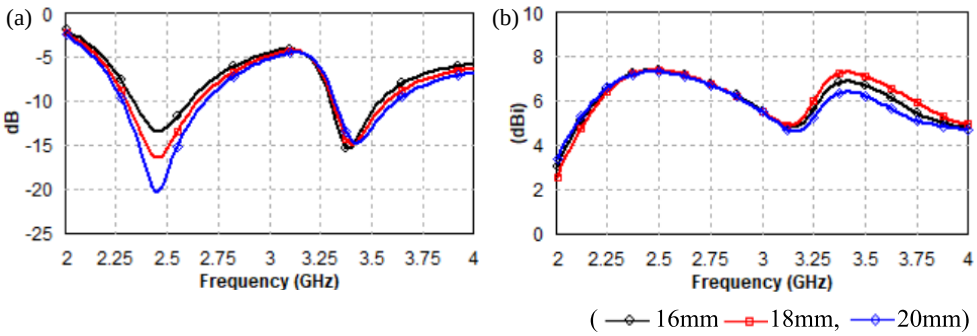

FIGURE 8. (a) S_{11}. (b) Gain for different AMC surface heights.

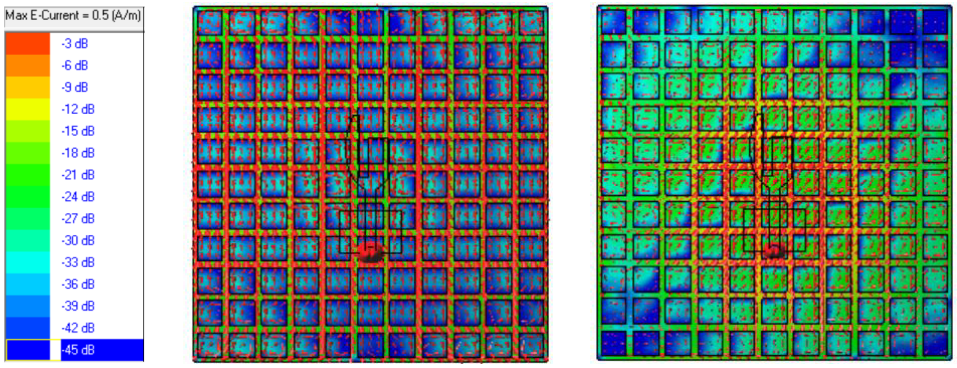

FIGURE 9. Scalar and vector surface current density distributions on the AMC surface.

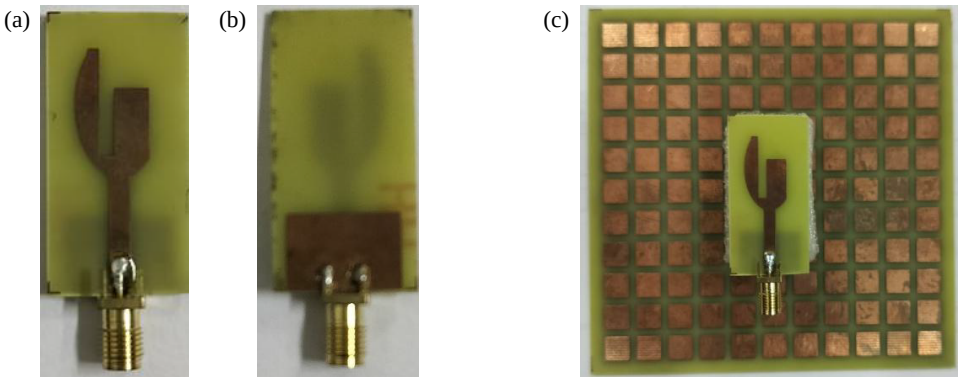

FIGURE 10. (a) Top view, (b) bottom view of monopole antenna, (c) antenna with AMC.

than in the lower band of the antenna with the AMC surface as a cross-polar component more in the upper band of the monopole antenna.

3.3. Fabrication and Measurement Results

The optimized monopole antenna and AMC surface are fabricated (Fig. 10) to validate the simulated results. The Agilent Field Fox N9116A Vector Network Analyzer (VNA) is used to measure S_{11} in an anechoic chamber. The VNA, along with the cable and connector/adaptor connecting it to the antenna port, is calibrated to mitigate measurement errors and ensure the accuracy of S_{11} measurements.

A standard horn antenna is used in an anechoic chamber to measure the radiation patterns in the far-field region. The proposed antenna under test (AUT), a receiving antenna, is connected to the 9916A Agilent Field Fox spectrum analyzer, and the standard horn antenna, a transmitting antenna, is connected to a microwave source, the Agilent Field Fox network analyzer N9916A. The distance between the transmitting and receiving antennas is kept more than $2D^2/\lambda$; D is the maximum dimension of the antenna, and λ is the wavelength corresponding to the operating frequency. Friis' transmission equation is used to calculate the gain of the antenna. The connector and cable losses are considered in the gain calculation.

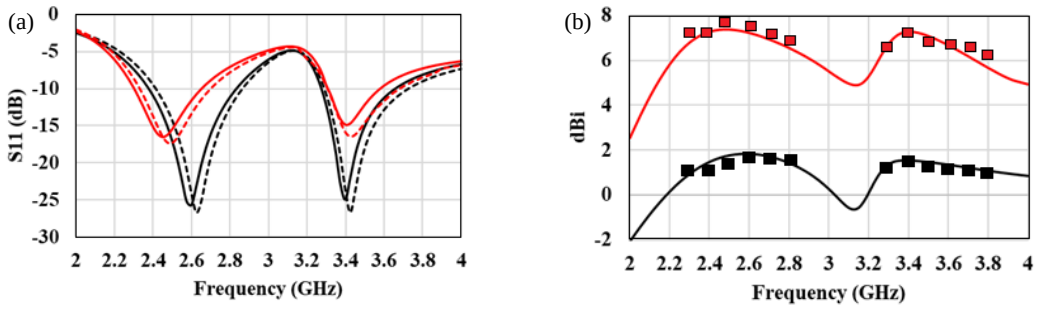

FIGURE 11. (a) Simulated and measured S_{11} with/without AMC. (b) Simulated and measured gain with/without AMC.

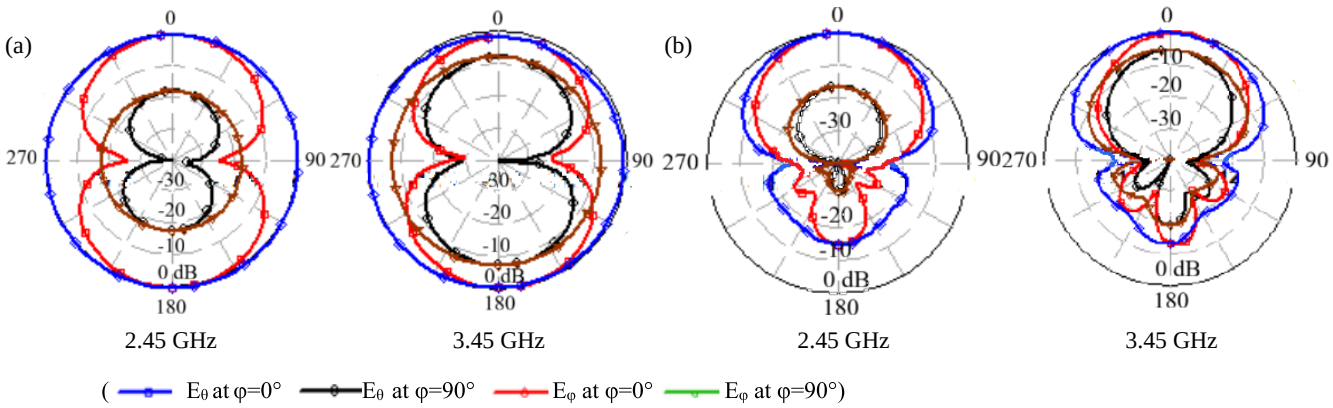

FIGURE 12. Measured radiation patterns, (a) without AMC, (b) with AMC.

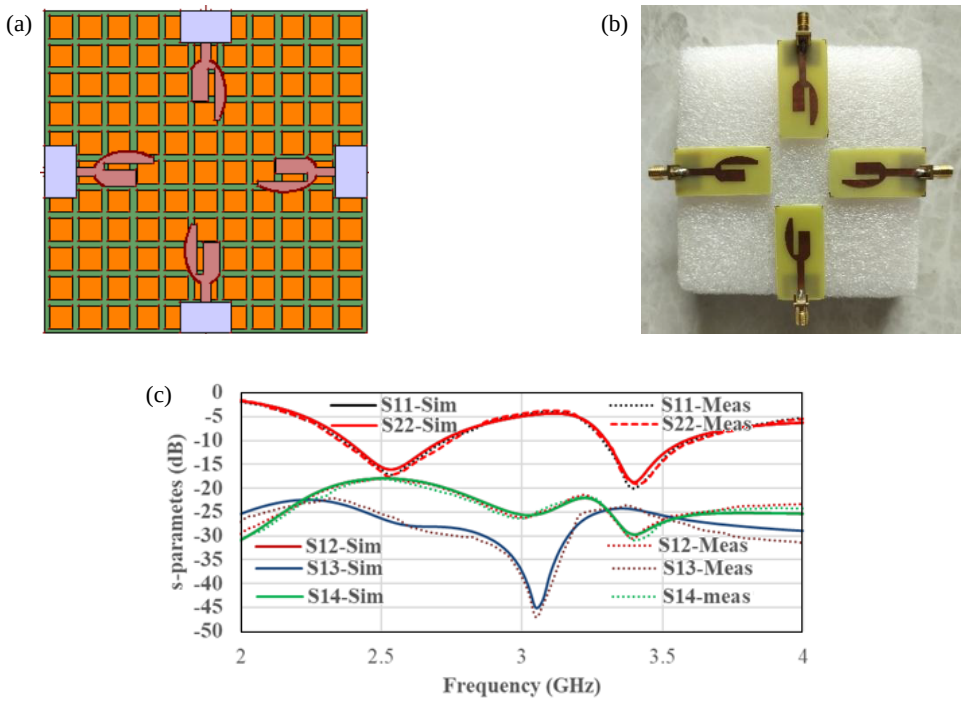

FIGURE 13. (a) Geometry. (b) Fabricated MIMO antenna. (c) S-parameters of MIMO antenna.

The measured S_{11} (Fig. 11(a)) and antenna gain (Fig. 11(b)) are compared with the simulated results. The measured results verify the simulated ones. The in-phase reflection of the AMC surface results in an improvement of 5.5 dB. The monopole antenna radiates the fields, but also causes the blockage of the reflected fields. Therefore, a small monopole antenna offers higher gain improvement. The gain improvement decreases as the dimensions of the monopole antenna increase due to blockage. Fig. 12 depicts the measured radiation patterns of the monopole antenna with and without the AMC surface. The

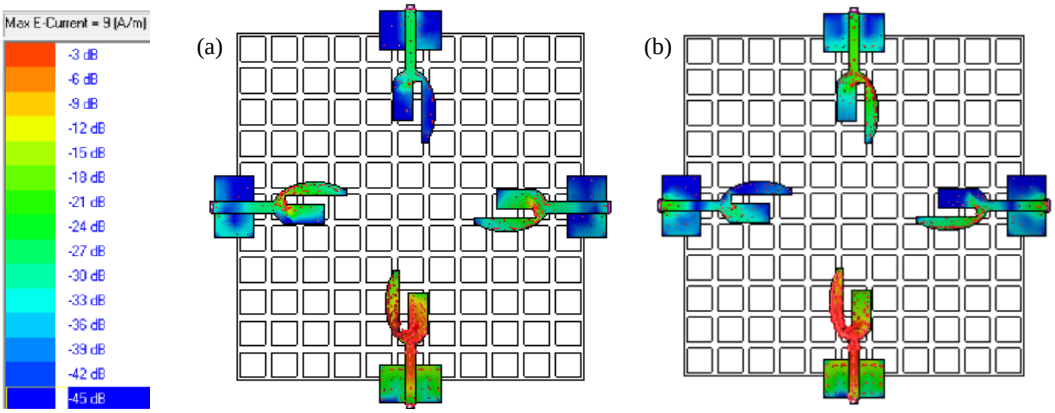

FIGURE 14. Surface current distribution of MIMO antenna. (a) 2.45 GHz, (b) 3.45 GHz.

TABLE 1. Comparison with the latest reported antennas.

Ref.	Monopole Antenna (mm^3)	Reflector Surface	Antenna with reflector (mm^3)	Operating Bands GHz	Electrical size ($\lambda_0 \times \lambda_0 \times \lambda_0$)	Peak Gain dBi
[13]	$30 \times 30 \times 1.6$	FSS	$62.5 \times 63 \times 25$	3–12	$0.625 \times 0.63 \times 0.25$	8.3
[16]	$100 \times 70 \times 1.0$	FSS	$80 \times 80 \times 17$	2.3–2.65 4.9–6.45	$0.6 \times 0.6 \times 0.13$	6.8 9.0
[17]	$21 \times 12.8 \times 1.6$	FSS	$70 \times 70 \times 12$	3.2–3.7 5.15–5.5	$0.746 \times 0.746 \times 0.128$	8.0 8.3
[18]	$28 \times 36 \times 1.6$	AMC	$79.9 \times 79.9 \times 8$	2.37–2.5 4.45–4.9	$0.63 \times 0.63 \times 0.064$	5 7.5
[20]	$12 \times 8 \times 0.64$	Plane metallic	$24 \times 16 \times 9$	27.3–29 36–42	$2.184 \times 1.45 \times 0.819$	7.96 8.2
This work	$16 \times 29.4 \times 1.6$	AMC	$100 \times 100 \times 18$	2.35–2.7 3.3–3.6	$0.78 \times 0.78 \times 0.166$	7.5 7.4

omnidirectional radiation pattern of the dual-band antenna becomes directional with the application of the AMC surface. The cross polarization is more at 3.45 GHz than 2.5 GHz due to the significant increase in the horizontal electric field component at 3.45 GHz.

4. FOUR ELEMENT HIGH-GAIN DUAL-BAND MIMO ANTENNA

A four-element MIMO antenna is designed by placing an element above the center of each side of a 100 mm × 100 mm AMC surface at a height of 18 mm (Fig. 13(a)). The elements are placed orthogonally. Therefore, spatial and orthogonal diversity techniques are used to achieve isolation in a high-gain dual-band antenna using a common AMC surface. The antenna offers isolations > 18 dB and > 22 dB over the lower and higher bands, respectively. Thus, a simple high-gain MIMO antenna with high isolation is designed without using any complicated isolation techniques. The fabricated MIMO antenna is depicted in Fig. 13(b). The measured and simulated S-parameters are shown in Fig. 13(c). As the MIMO structure is symmetrical, negligible variation is observed in $S_{11}/S_{22}/S_{33}/S_{44}$. Therefore, S_{11}, S_{22}, S_{12}, S_{13}, and S_{14} are shown in Fig. 13(c). S_{11} and S_{22} overlap with each other. Similarly, S_{13} and S_{14} overlap because of symmetry.

The scalar and vector surface current distributions at 2.5 GHz and 3.45 GHz (Fig. 14) illustrate the coupling between the elements of the MIMO antenna. The bottom antenna element is excited, whereas the other three are matched-terminated. The surface current density induced at 2.5 GHz, in the adjacent elements (left and right), is higher than that in the top element. Thus, $S_{12} = S_{14} > S_{13}$. Due to the increased electrical distance between the elements, the surface current density at 3.45 GHz is lower than that at 2.45 GHz. As a result, higher isolation is achieved at 3.45 GHz.

The radiation patterns are measured by exciting one port at a time, with the other three ports matched-terminated. The measured radiation patterns of the MIMO structures (Fig. 15) are stable, orthogonally polarized, and broadside-directed. The front-to-back lobe ratio is less as the elements are placed above the edge of the AMC surface.

4.1. MIMO System Performance Parameters

A MIMO antenna system offers a multichannel system; therefore, it must satisfy certain MIMO performance parameters, such as Envelope Correlation Coefficient (ECC), Total-Active Reflection coefficient (TARC), Directive Gain (DG), and Mean Effective Gain (MEG) to ensure proper functioning of the

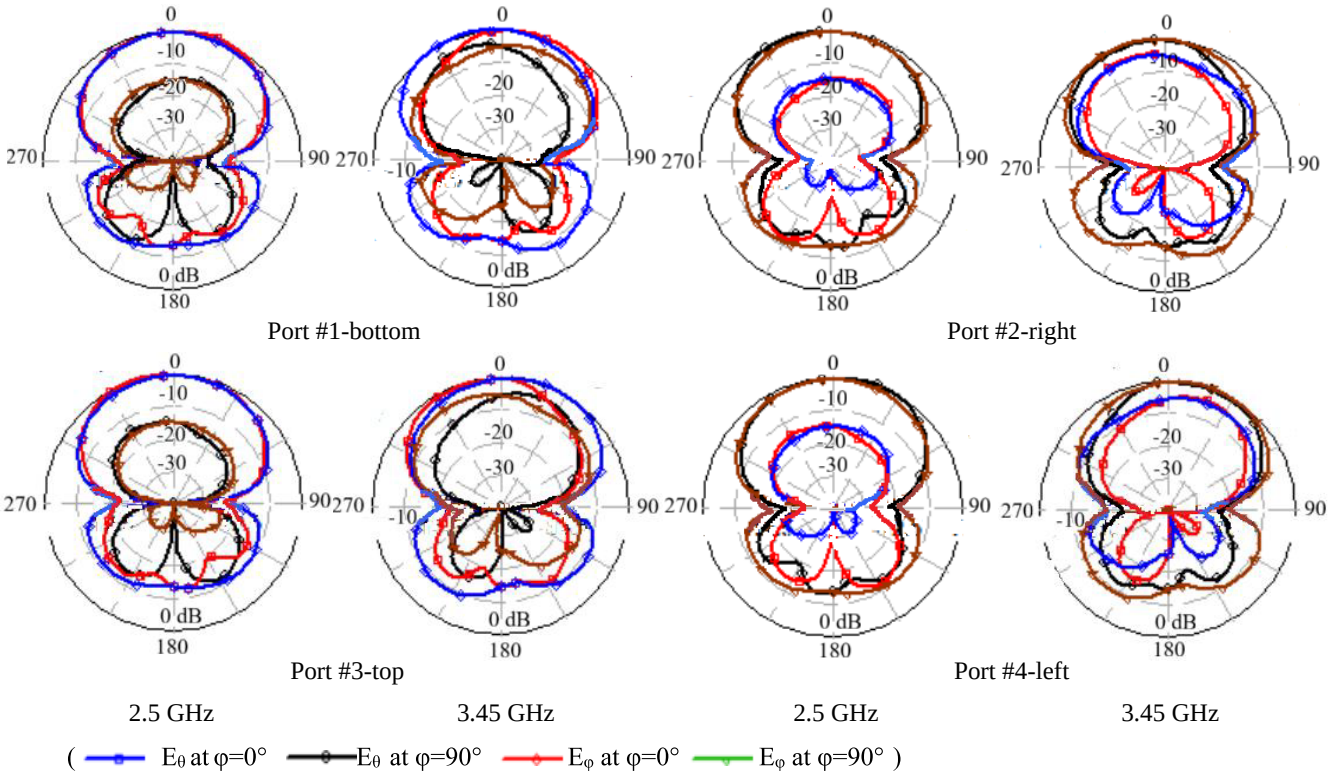

FIGURE 15. Measured radiation patterns of high-gain MIMO antenna.

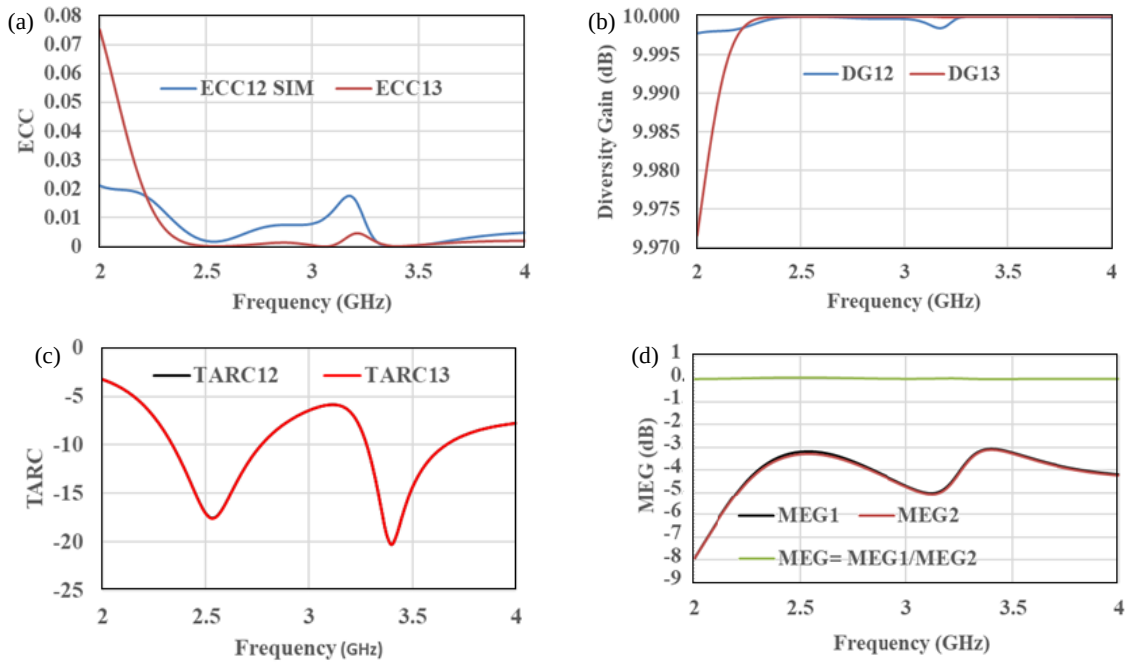

FIGURE 16. Performance parameters of MIMO antenna. (a) ECC, (b) DG, (c) TARC, (d) MEG.

MIMO system [21–25]. These MIMO parameters are analyzed for the proposed dual-band high-gain MIMO antenna system.

The ECC (ECC12 is between element-1 (bottom) and element-2 (right), and ECC13 is between element-1 and element-3 (top)) of the proposed MIMO structure is < 0.02 over the lower (2.3–2.7 GHz) and upper (3.3–3.6 GHz) bands. The ECC is less than the standard ECC of 0.5. The diversity gain (DG12 and DG13) is calculated. It is more than 9.998 dB over both the bands. A DG close to 10 dB substantiates the performance of the MIMO antenna. The MEGs (MEG1 and MEG2) of close-by elements are nearly equal; therefore, MEG1/MEG2 is approximately 0 dB. ECC, DG,

MEG, and TARC adhere to and satisfy the MIMO antenna's specifications. These performance parameters are shown in Fig. 16.

5. COMPARISON WITH STATE-OF-THE-ART ANTENNAS

In Table 1, the dual-band high-gain antenna is compared with the latest antennas in terms of the technique used, monopole dimensions, overall antenna size with a reflector, operating bands, and peak gain. The structures in [13, 16, 17] have employed FSS, while [18, 19] have used AMC, and [20] has utilized a plane metallic reflector. Refs. [13, 20] have a higher profile than our antenna. Refs. [16, 17] are smaller in size, but [16] offers less gain in the lower band, whereas [17] has a slightly higher gain due to the larger monopole dimensions than our antenna. Ref. [18] provides a lower gain than our antenna. The designed antenna has significantly smaller monopole dimensions, resulting in less blockage and greater gain improvement. Our antenna has a low cost, is easy to design, and supports the 4-element high-gain MIMO operation for Bluetooth, Wi-Fi, and 5G bands.

6. CONCLUSION

A compact dual-band antenna is designed from an elliptical monopole by selectively etching a symmetrical portion of an ellipse and adding a rectangular strip to the etched elliptical monopole. The dimensions of the ground plane are reduced, and the gap between the monopole and ground plane is increased to ensure that the monopole is excited in the fundamental mode. An AMC reflecting surface is designed and placed below the monopole to enhance the antenna gain. A MIMO antenna is designed by placing the antenna elements above the four edges of the AMC surface. The $0.78\lambda_0 \times 0.78\lambda_0 \times 0.166\lambda_0$ antenna provides the maximum gain of 7.5 dBi over the lower band and 7.4 dBi over the upper band, with λ_0 being the free-space wavelength at 2.35 GHz.

REFERENCES

[1] Kumar, G. and K. P. Ray, *Broadband Microstrip Antennas*, Artech House, Norwood, MA, 2003.

[2] Kumar, O. P., P. Kumar, T. Ali, P. Kumar, and S. Vincent, "Ultrawideband antennas: Growth and evolution," *Micromachines*, Vol. 13, No. 1, 60, 2022.

[3] Singh, P. P., S. K. Sharma, and N. Gupta, "Design and performance analysis of a dual band patch antenna and its MIMO implementation for Wi-Fi, Radar, and V2X applications," *Advanced Electromagnetics*, Vol. 14, No. 2, 35–44, 2025.

[4] Woo, D. S., "A triple band C-shape monopole antenna for vehicle communication application," *Progress In Electromagnetics Research C*, Vol. 121, 97–106, 2022.

[5] Thiruvenkadam, S. and E. Parthasarathy, "Compact multiband monopole antenna design for IoT applications," *Journal of Electromagnetic Waves and Applications*, Vol. 37, No. 5, 629–643, 2023.

[6] El Hadri, D., A. Zugari, A. Zakriti, M. El Ouahabi, and M. Taouzari, "A compact triple band antenna for military satellite communication, radar and fifth generation applications," *Advanced Electromagnetics*, Vol. 9, No. 3, 66–73, 2020.

[7] Salim, A. J., J. K. Mohammed, H. Al-Saedi, and J. K. Ali, "A proximity-fed multi-band printed antenna for wireless communication applications," *Progress In Electromagnetics Research C*, Vol. 145, 153–165, 2024.

[8] Jing, J., J. Pang, H. Lin, Z. Qiu, and C.-J. Liu, "A multiband compact low-profile planar antenna based on multiple resonant stubs," *Progress In Electromagnetics Research Letters*, Vol. 94, 1–7, 2020.

[9] Verulkar, S. M., A. Khade, M. Trimukhe, and R. K. Gupta, "Dual band split ring monopole antenna structures for 5G and WLAN applications," *Progress In Electromagnetics Research C*, Vol. 122, 17–30, 2022.

[10] Ran, X., Z. Yu, T. Xie, Y. Li, X. Wang, and P. Huang, "A novel dual-band binary branch fractal bionic antenna for mobile terminals," *International Journal of Antennas and Propagation*, Vol. 2020, No. 1, 6109093, 2020.

[11] Wang, L., J. Yu, T. Xie, and K. Bi, "A novel multiband fractal antenna for wireless application," *International Journal of Antennas and Propagation*, Vol. 2021, No. 1, 9926753, 2021.

[12] Al-Gburi, A. J. A., I. M. Ibrahim, Z. Zakaria, M. K. Abdulhameed, and T. Saeidi, "Enhancing gain for UWB antennas using FSS: A systematic review," *Mathematics*, Vol. 9, No. 24, 3301, 2021.

[13] Din, I. U., S. Ullah, S. I. Naqvi, R. Ullah, S. Ullah, E. M. Ali, and M. Alibakhshikenari, "Improvement in the gain of UWB antenna for GPR applications by using frequency-selective surface," *International Journal of Antennas and Propagation*, Vol. 2022, No. 1, 2002552, 2022.

[14] Daira, S. E. I., M. Lashab, H. A. Berkani, M. Belattar, I. Gharbia, and R. A. Abd-Alhameed, "A curved single-layer FSS design for gain improvement of a compact size CPW-fed UWB monopole antenna," *Microwave and Optical Technology Letters*, Vol. 66, No. 1, e33943, 2024.

[15] Nakmouche, M. F., A. M. M. A. Allam, D. E. Fawzy, and D.-B. Lin, "Development of a high gain FSS reflector backed monopole antenna using machine learning for 5G applications," *Progress In Electromagnetics Research M*, Vol. 105, 183–194, 2021.

[16] Shi, C., J. Zou, J. Gao, and C. Liu, "Gain enhancement of a dual-band antenna with the FSS," *Electronics*, Vol. 11, No. 18, 2882, 2022.

[17] Verulkar, S. M., A. Rochkari, M. Trimukhe, V. Bodade, and R. Gupta, "High gain compact dual band antenna using frequency selective surface for 5G and WLAN applications," *Progress In Electromagnetics Research C*, Vol. 142, 1–11, 2024.

[18] Abdelghany, M. A., M. F. A. Sree, A. Desai, and A. A. Ibrahim, "Gain improvement of a dual-band CPW monopole antenna for sub-6 GHz 5G applications using AMC structures," *Electronics*, Vol. 11, No. 14, 2211, 2022.

[19] Aggarwal, I., S. Pandey, and M. R. Tripathy, "A high gain super wideband metamaterial based antenna," *Journal of Microwaves, Optoelectronics and Electromagnetic Applications*, Vol. 20, No. 2, 248–273, Jun. 2021.

[20] Mohammed, D. Z. and A. J. A. Al-Gburi, "Compact, gain-enhanced 5G mmWave antenna with metallic ground-backed reflector for high-speed railway communication systems," *High-speed Railway*, Vol. 3, No. 4, 281–292, 2025.

[21] Sharma, U., G. Srivastava, M. K. Khandelwal, and R. Roges, "Design challenges and solutions of multiband MIMO antenna for 5G/6G wireless applications: A comprehensive review," *Progress In Electromagnetics Research B*, Vol. 104, 69–89, 2024.

[22] Srinubabu, M. and N. V. Rajasekhar, "A compact and efficiently designed two-port MIMO antenna for N78/48 5G applications," *Heliyon*, Vol. 10, No. 7, e28981, 2024.

[23] Deshmukh, A. A., S. D. Nawale, V. R. Kapure, S. A. Deshmukh, M. A. Trimukhe, and R. K. Gupta, "Highly isolated compact dual-band MIMO antenna using stubs, slots and neutralization line for 5G Wi-MAX and WLAN applications," *Progress In Electromagnetics Research C*, Vol. 158, 27–35, 2025.

[24] Kulkarni, J., C.-Y.-D. Sim, R. K. Gangwar, and J. Anguera, "Broadband and compact circularly polarized MIMO antenna with concentric rings and oval slots for 5G application," *IEEE Access*, Vol. 10, 29 925–29 936, 2022.

[25] Verulkar, S. M., A. Khade, M. A. Trimukhe, and R. K. Gupta, "Compact wideband four elements MIMO antenna for 5G applications," *Progress In Electromagnetics Research C*, Vol. 137, 199–209, 2023.

[26] Graham, A. M., S. N. Daskalakis, V. Fusco, M. M. Tentzeris, and S. D. Asimonis, "A highly efficient, scalable, tetra-band metamaterial-based ambient RF energy harvester," *IEEE Transactions on Microwave Theory and Techniques*, Vol. 73, No. 9, 6787–6798, 2025.